Scientific Research Publishing

Open Journal of Applied Sciences, 2026, 16(11), 4503-4521
https://www.scirp.org/journal/ojapps
ISSN Online: 2165-3925
ISSN Print: 2165-3917

Ionospheric Irregularities at the Koudougou GNSS Station during 2010-2016: Occurrence and Associated Interplanetary Conditions

Abidina Diabaté[1,2,3], M'Bi Kaboré[1,2,3], Boureima Sombié[3], Karim Guibula[3,4], Thierno Madani Sidibé[5]

[1]Physics Department, Nazi Boni University, Bobo-Dioulasso, Burkina Faso
[2]Laboratory of Materials, Heliophysics and Environment (La.M.H.E), Nazi Boni University, Bobo-Dioulasso, Burkina Faso
[3]Laboratory of Analytical Chemistry, Space Physics and Energy (L@CAPSE), Norbert Zongo University, Koudougou, Burkina Faso
[4]Physics Department, Virtual University of Burkina Faso, Ouagadougou, Burkina Faso
[5]Laboratory of Hybrid and Renewable Energies (HREL), Faculty of Sciences and Technologies of Bamako (FST/USTTB), Bamako, Mali
Email: kariguib92@gmail.com

How to cite this paper: Diabaté, A., Kaboré, M., Sombié, B., Guibula, K. and Sidibé, T.M. (2026) Ionospheric Irregularities at the Koudougou GNSS Station during 2010-2016: Occurrence and Associated Interplanetary Conditions. *Open Journal of Applied Sciences*, **16**, 4503-4521.
https://doi.org/10.4236/ojapps.2026.1611246

Received: September 29, 2026
Accepted: November 16, 2026
Published: November 19, 2026

Copyright © 2026 by author(s) and Scientific Research Publishing Inc.
This work is licensed under the Creative Commons Attribution International License (CC BY 4.0).
http://creativecommons.org/licenses/by/4.0/

Open Access

Abstract

Equatorial ionospheric irregularities constitute an important component of ionospheric variability, with a particularly pronounced occurrence during nighttime. This study aims to characterize their occurrence and distribution, as well as the interplanetary conditions associated with these episodes, at Koudougou GNSS station, Burkina Faso. Ionospheric irregularities were identified from ROTI data derived from RINEX observations over the 2010-2016 period. An irregularity was defined when the global ROTI reached or exceeded 0.5 TECU/min, and episodes were classified as moderate or strong according to their maximum ROTI value. The geomagnetic context was characterized using the Aa and aa indices, while interplanetary conditions were analyzed using B_{mag}, B_z, solar wind speed, and dynamic pressure. Irregularities were observed on 1107 of the 1757 days with available data, corresponding to an occurrence frequency of 63.00%. Occurrences were predominantly nighttime (82.57%) and mainly concentrated between 18:00 and 02:00 LT. The largest proportions of days with ionospheric irregularities occurred in spring (30.26%) and autumn (27.55%), which together accounted for 57.81% of the irregularity days. Superposed Epoch analysis (SEA) showed, for both moderate and strong episodes, a systematic organization of solar-wind parameters according to geomagnetic context: B_{mag}, solar wind speed, and dynamic pressure increased from quiet to disturbed conditions, whereas B_z evolved from

positive toward more negative values. These results characterize the occurrence and distribution of ionospheric irregularities at Koudougou and the interplanetary conditions associated with their occurrence.

Keywords

Ionospheric Irregularities, ROTI Index, Solar Win, Geomagnetic Context

1. Introduction

Space weather encompasses variations in the physical conditions of the near-Earth space environment and their effects on geophysical and technological systems. The ionosphere is very sensitive to these variations because of its ionized state and its strong coupling to electric and magnetic fields. Ionospheric disturbances can affect radio-wave propagation and degrade the performance of communication, navigation, and positioning systems, including Global Navigation Satellite Systems (GNSS) [1]. Characterizing and understanding ionospheric variability is therefore important for investigating Sun-Earth relationships and assessing the effects of space weather on technological systems.

At low latitudes, ionospheric dynamics are strongly influenced by interactions among the solar wind, magnetosphere, and ionosphere, as well as by electrodynamic processes characteristic of the equatorial region [2] [3]. These processes influence the vertical $E \times B$ drift and the dynamics of the equatorial F region. After sunset, the prereversal enhancement of the zonal electric field can promote the upward drift and uplift of the F region, creating favorable conditions for the development of the Rayleigh-Taylor instability [4] [5]. This instability can lead to the formation of low-density plasma structures, commonly referred to as plasma bubbles, which are associated with electron-density irregularities in the F region [2] [6]. These irregularities can produce strong fluctuations in electron content and degrade GNSS signal quality through ionospheric scintillation [7].

The occurrence of equatorial ionospheric irregularities exhibits substantial spatial and temporal variability. Its occurrence depends on several factors, including local time, season, solar activity, longitude, and geomagnetic conditions [8]. Observations from different equatorial regions generally show higher occurrence during the post-sunset period, together with pronounced seasonal variability, often around the equinoxes. This variability reflects the complexity of equatorial electrodynamics and the influence of multiple geophysical factors operating over different spatial and temporal scales. Characterizing this variability is therefore essential for describing the conditions under which ionospheric irregularities develop.

The increasing use of GNSS provides an effective means of investigating these phenomena through measurements of variations in Total Electron Content (TEC). TEC can be estimated from GNSS observations and represents the inte-

grated electron density along the satellite-receiver signal path. Among the indices derived from TEC, the Rate Of TEC Index (ROTI) is widely used to characterize rapid fluctuations in TEC and to detect ionospheric irregularities [9]. This approach is particularly useful in Africa, where GNSS observations enable long-term investigations of ionospheric irregularities in regions where complementary measurements of electrodynamic parameters and scintillation may be limited. Several studies have demonstrated the usefulness of ROTI for characterizing the variability of ionospheric irregularities in East and West Africa [10]-[13].

In West Africa, several studies have contributed to the characterization of TEC variability and ionospheric irregularities using GNSS observations. Studies have been conducted in Burkina Faso and other equatorial regions of Africa using different observational techniques and ionospheric indicators [14]-[18]. Together, these studies highlight substantial variability in ionospheric activity across observation sites and under different geophysical conditions. However, the climatology of ionospheric irregularities in West Africa, particularly their systematic association with interplanetary conditions, remains less extensively documented than in some other equatorial regions. In particular, further investigation is needed to characterize the association of ionospheric irregularities with solar-wind parameters in the West African context.

The Koudougou GNSS station (12˚15'N, 2˚20'W, Burkina Faso) within the equatorial region of West African (Sawadogo *et al*., 2023), offers a suitable site for investigating ionospheric irregularities. In this study, we analyze observations from this station during the 2010-2016 period to characterize, first, the occurrence and distribution of ionospheric irregularities in terms of their intensity, local time, and season. We then examine the interplanetary conditions associated with irregularity episodes by considering B_{mag}, B_z, solar-wind speed V, and dynamic pressure P_{dyn} under different geomagnetic conditions. By combining GNSS/ROTI observations with geomagnetic context and interplanetary parameters, this study aims to provide a climatological characterization of ionospheric irregularities at Koudougou and document their association with solar-wind conditions, thereby contributing to the understanding of their variability in West Africa.

2. Data and Methodology

2.1. Data

In this study, three complementary datasets were used: ROTI data, solar wind parameters, and the geomagnetic index aa.

The ROTI (Rate of TEC Index) values, used as an indicator of ionospheric irregularities, were obtained by processing the raw RINEX (Receiver Independent Exchange Format) files from the Koudougou GNSS station, located at 12˚15'N and 2˚20'W. The available data cover the period 2009-2017. The period retained for the analyses presented in this study is 2010-2016.

The solar wind parameters, used to characterize the interplanetary conditions associated with ionospheric irregularity episodes, were obtained from the OMNI-

Web database at a temporal resolution of one minute. They include the interplanetary magnetic field magnitude, denoted B_{mag}, its B_z component in GSM coordinates, the solar wind speed V, and the dynamic pressure P_{dyn}. This data was downloaded from https://omniweb.gsfc.nasa.gov/form/omni_min.html?utm_source=chatgpt.com.

The geomagnetic index aa, available at a temporal resolution of 3 hours, was used to characterize the geomagnetic conditions associated with ionospheric irregularities. The data were obtained from the international Service of Geomagnetic Indices (ISGI) from the link: https://isgi.unistra.fr/data_download.php?utm_source=chatgpt.com.

2.2. Methodology

2.2.1. Determination of ROTI and Identification of Ionospheric Irregularities

1) Determination of ROTI index

In this study, preprocessed ROTI (Rate Of TEC Index) values were used as an indicator of ionospheric irregularities. ROTI is a widely adopted metric for characterizing ionospheric plasma density fluctuations and was originally introduced by [9]. Data processing was performed using the software package provided by GIRGEA (Groupement de Recherche International en Géophysique Europe-Afrique), available on its website https://www.girgea.org/.

First, the ROT (Rate Of TEC), which represents the temporal rate of change of the Total Electron Content (TEC), was computed from the temporal gradient of the Slant TEC (STEC) derived from carrier-phase observations in 30-s RINEX files:

$$\mathrm{ROT} = \frac{\mathrm{STEC}_{k+1} - \mathrm{STEC}_k}{t_{k+1} - t_k} \times 60 \tag{1}$$

where STEC_k and STEC_{k+1} denote STEC values (in TECU) at epochs t_k and t_{k+1}, respectively, and $\left(t_{k+1} - t_k\right)$ is the time interval between two consecutive observations (30 s in this study).

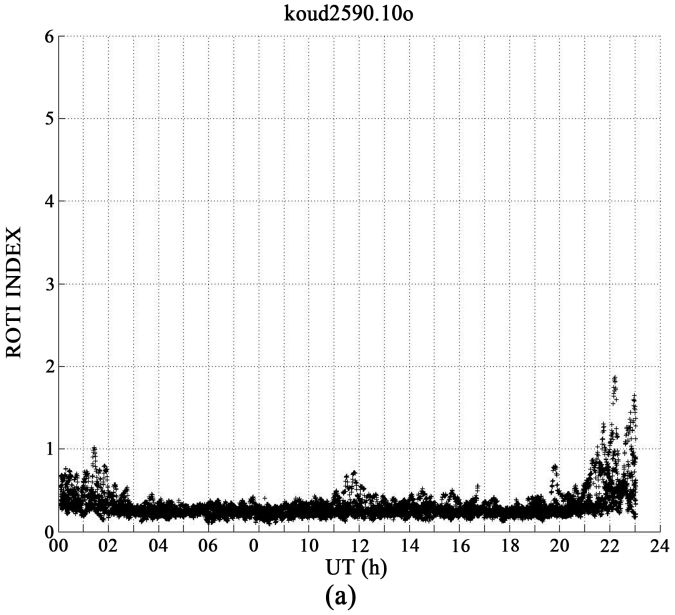
The ROTI index was subsequently calculated as the standard deviation of ROT values over a sliding time window of 10 min, corresponding to 20 ROT samples, according to:

$$\mathrm{ROTI} = \sqrt{\left\langle \mathrm{ROT}^2 \right\rangle - \left\langle \mathrm{ROT} \right\rangle^2} \tag{2}$$

where $\langle \cdot \rangle$ denotes the arithmetic mean computed over the considered 10 min window. The resulting ROTI values are expressed in TECU/min.

Following established GNSS data-quality criteria, a 20˚ elevation mask was applied to reduce the effects of multipath propagation and low-elevation observation errors [19].

Figure 1 presents examples of the graphical (**Figure 1(a)**) and numerical (**Figure 1(b)**) output files generated for 16 August 2010 (DOY 259), illustrating the ROTI data used in this study.



(a)

roti_koud2590.txt

prn	temps(s)	tec_phi	tec_code	sub_lat	sub_lon	elev	VTEC	temps(s)	ind_roti
2.00	6030.0	39.602	39.642	16.687	353.487	30.196	11.41	6330.0	0.245
2.00	6060.0	39.670	39.539	16.651	353.506	30.389	11.49	6360.0	0.251
2.00	6090.0	39.728	39.436	16.614	353.524	30.582	11.57	6390.0	0.257
2.00	6120.0	39.682	39.335	16.578	353.543	30.775	11.58	6420.0	0.268
2.00	6150.0	39.499	39.235	16.543	353.561	30.967	11.51	6450.0	0.261
2.00	6180.0	39.598	39.137	16.507	353.579	31.160	11.61	6480.0	0.256
2.00	6210.0	39.483	39.039	16.472	353.597	31.352	11.59	6510.0	0.258
2.00	6240.0	39.776	38.942	16.437	353.615	31.544	11.80	6540.0	0.216
2.00	6270.0	39.663	38.846	16.402	353.632	31.736	11.78	6570.0	0.223
2.00	6300.0	39.658	38.751	16.367	353.649	31.928	11.82	6600.0	0.226
2.00	6330.0	39.530	38.657	16.333	353.666	32.119	11.78	6630.0	0.249
2.00	6360.0	39.431	38.565	16.299	353.683	32.311	11.76	6660.0	0.258
2.00	6390.0	39.187	38.473	16.265	353.700	32.502	11.65	6690.0	0.264
2.00	6420.0	39.242	38.382	16.231	353.716	32.693	11.73	6720.0	0.287
2.00	6450.0	39.406	38.292	16.197	353.732	32.884	11.87	6750.0	0.288
2.00	6480.0	39.408	38.203	16.164	353.748	33.074	11.91	6780.0	0.285
2.00	6510.0	39.294	38.115	16.131	353.764	33.264	11.88	6810.0	0.324
2.00	6540.0	39.250	38.028	16.098	353.779	33.454	11.89	6840.0	0.344
2.00	6570.0	39.384	37.942	16.065	353.795	33.644	12.02	6870.0	0.330
2.00	6600.0	39.417	37.857	16.032	353.810	33.834	12.08	6900.0	0.336
2.00	6630.0	39.459	37.773	16.000	353.825	34.023	12.14	6930.0	0.355
2.00	6660.0	39.301	37.690	15.968	353.839	34.212	12.08	6960.0	0.372
2.00	6690.0	39.430	37.607	15.936	353.854	34.401	12.21	6990.0	0.344
2.00	6720.0	39.239	37.526	15.904	353.868	34.589	12.12	7020.0	0.387
2.00	6750.0	39.136	37.445	15.872	353.883	34.778	12.10	7050.0	0.407

(b)

Figure 1. Examples of output files generated from Koudougou GNSS data for 16 August 2010 (DOY 259). (a) Graphical representation of ROTI variations as a function of Universal Time (UT); (b) corresponding numerical output file containing the computed ROTI values.

2) Identification of ionospheric irregularities

For each daily ROTI file within the 2010-2016 analysis period, the PRN, ROTI time, and ROTI value were extracted and subsequently concatenated across all available files. The resulting observations were sorted chronologically and grouped by time. At each 30-s epoch, a global ROTI value was defined as the maximum ROTI among the available satellites. This global ROTI time series was then used to identify and catalogue ionospheric irregularity episodes. An irregularity was identified when the global ROTI reached or exceeded 0.5 TECU/min, a threshold used in recent GNSS/ROTI-based studies to characterize ionospheric disturbances [20] An irregularity episode was defined as a continuous period during which the global ROTI remained at or above the threshold. Two successive episodes were considered distinct when the interruption between two periods of activity exceeded 15 min. Episodes were classified according to their intensity into two categories, following the ROTI ranges reported by [21], but with a slight adaptation using the maximum ROTI value reached during each episode ($\mathrm{ROTI}_{\max}$): moderate, for $0.5 \le \mathrm{ROTI}_{\max} \le 1\,\mathrm{TECU/min}$, and strong, for $\mathrm{ROTI}_{\max} > 1\,\mathrm{TECU/min}$. This criterion was used to distinguish episodes while avoiding artificial fragmentation of a single irregularity sequence.

In the study of ionospheric irregularity occurrences, daily classification was determined according to the highest irregularity intensity recorded during the day. Consequently, any day exhibiting at least one intense irregularity event ($\mathrm{ROTI} > 1\,\mathrm{TECU/min}$) was categorized as an intense ionospheric irregularity day, regardless of the simultaneous occurrence of moderate irregularity events ($0.5 \le \mathrm{ROTI} \ge 1\,\mathrm{TECU/min}$).

2.2.2. Data Availability and Climatological Analysis of Ionospheric Irregularities

Before the climatological analysis, an assessment of data availability was performed. A day for which no ROTI measurement was available was considered a gap day, corresponding to a complete interruption of observations. A day containing ROTI observations, whether covering the entire day or only part of it, was considered an available day. This classification was used to assess the temporal continuity and observational coverage of the dataset.

The climatological variability of ionospheric irregularities was investigated using the daily files. The observations were grouped into four seasons: winter (December-February), spring (March-May), summer (June-August), and autumn (September-November). Daily variability was also examined by distinguishing between the daytime period (06:00 - 18:00 local time) and the nighttime period (18:00 - 06:00 local time).

For the characterization of the geomagnetic conditions associated with individual days, the daily geomagnetic index Aa was used. Days with $Aa < 20$ nT were classified as quiet days, whereas days with $Aa \geq 20$ nT were classified as disturbed days [22]-[24]. This daily classification was used to examine the geomagnetic context of ionospheric irregularities in the climatological analysis.

2.2.3. Superposed Epoch Analysis (SEA)

To characterize the interplanetary conditions associated with ionospheric irregularity episodes, a Superposed Epoch Analysis (SEA) was applied to the identified episodes. This approach consists of superimposing time series with respect to a common reference epoch in order to identify their average temporal evolution.

For each episode, the beginning of the episode was defined as the reference epoch t_0. The interplanetary parameter time series were then extracted over a temporal window extending from $t_0 - 12$ h to $t_0 + 12$ h, with a temporal resolution of one minute, yielding 1441 time points per episode.

The parameters considered were the interplanetary magnetic field magnitude (B_{mag}), its B_z component in GSM coordinates, the solar wind speed V, and the dynamic pressure P_{dyn}.

For each episode, the OMNI data were aligned with the event time scale. Some episode start times could contain seconds other than zero. To ensure consistent temporal matching between the irregularities episodes and the OMNI data, we adopted the following rule: times at :00 and :01 were assigned to the same minute, times at :30 to the preceding minute, and time :31 the following minute. The aligned time series were then superposed within each episode category. At each relative time $t - t_0$, the mean and standard deviation were calculated from the available observations:

$$\bar{X}(t) = \frac{1}{N_t} \sum_{i=1}^{N_t} X_i(t) \tag{3}$$

where N_t denotes the number of available observations at the considered time. Missing values were excluded from the calculation of the means and standard de-

viations. The resulting mean profiles were represented together with envelopes corresponding to ±1 standard deviation.

The comparative analysis for each of two levels of irregularity intensity covered the three geomagnetic contexts. For moderate episodes, the comparisons focused on Moderate-quiet, Moderate-transition, and Moderate-disturbed. For strong episodes, the comparisons focused on Strong-quiet, Strong-transition and Strong-disturbed.

2.2.4. Geomagnetic Context

To characterize the geomagnetic context associated with each irregularity episode, a 6-h temporal window centered on t_0, from $t_0 - 3\,\text{h}$ to $t_0 + 3\,\text{h}$, was considered. The geomagnetic context was classified according to the aa index as follows:

- **Quiet geomagnetic conditions**: all aa values within the window were strictly below 20 nT;
- **Disturbed geomagnetic conditions**: all aa values within the window were greater than or equal to 20 nT;
- **Transition geomagnetic conditions**: the window contained both $aa < 20\,\text{nT}$ and $aa \geq 20\,\text{nT}$ values.

The 20 nT threshold was adopted from commonly used classifications of geomagnetic activity based on the aa/Aa index [22] [23]. Its application in the present study was adapted to the 3-h aa measurements and 6-h window centered on t_0.

Combining the geomagnetic classification with the ROTI-based intensity classification resulted in the six episode categories. The classification criteria based on the aa index and the ROTI threshold are summarized in Table 1.

Table 1. Classification of ionospheric irregularity episodes according to their intensity and geomagnetic context.

Episode categories	Condition on aa ($t_0 - 3\,\text{h}$ to $t_0 + 3\,\text{h}$)	Condition on ROTI
Moderate-quiet	$aa < 20\,\text{nT}$ all window	$0.5 \leq \text{ROTI}_{\max} \leq 1\,\text{TECU/min}$
Moderate-transition	Coexistence of $aa < 20\,\text{nT}$ & $aa \geq 20\,\text{nT}$	$0.5 \leq \text{ROTI}_{\max} \leq 1\,\text{TECU/min}$
Moderate-disturbed	$aa \geq 20\,\text{nT}$ all window	$0.5 \leq \text{ROTI}_{\max} \leq 1\,\text{TECU/min}$
Strong-quiet	$aa < 20\,\text{nT}$ all window	$\text{ROTI}_{\max} > 1\,\text{TECU/min}$
Strong-transition	$aa < 20\,\text{nT}$ and $aa \geq 20\,\text{nT}$	$\text{ROTI}_{\max} > 1\,\text{TECU/min}$
Strong-disturbed	$aa \geq 20\,\text{nT}$ all window	$\text{ROTI}_{\max} > 1\,\text{TECU/min}$

2.2.5. Statistical Analysis

The interplanetary conditions were compared between the different episode categories for B_{mag}, B_z, V, and P_{dyn}, and at each of the 1441 time instants within the [−12 h, +12 h] window.

At each time instant, the distributions of two populations (Quiet vs Transition or Disturbed vs Transition) being compared were assessed using a **two-sample Welch's t-test**. This test was preferred because it does not assume homogeneity of variances and remains robust in the presence of unequal sample size.

The Welch test statistic was calculated as:

$$t = \frac{\bar{X}_1 - \bar{X}_2}{\sqrt{\frac{s_1^2}{n_1} + \frac{s_2^2}{n_2}}} \tag{4}$$

were $\bar{X}_1$ and $\bar{X}_2$ are the sample means, s_1 and s_2 are the sample standard deviations, and n_1 and n_2 are the corresponding sample sizes. The degrees of freedom were estimated using the Welch-Satterthwaite approximation:

$$\upsilon = \frac{\left(\frac{s_1^2}{n_1} + \frac{s_2^2}{n_2}\right)^2}{\frac{\left(\frac{s_1^2}{n_1}\right)^2}{n_1 - 1} + \frac{\left(\frac{s_2^2}{n_2}\right)^2}{n_2 - 1}} \tag{5}$$

A nominal significance level of $\alpha = 0.05$ was adopted.

Because multiple comparisons were performed over the temporal window, the **Benjamini-Hochberg procedure** was applied to control the **False Discovery Rate (FDR)**. For m ordered p-values,

$$p_{(1)} \le p_{(2)} \le \cdots \le p_{(m)} \tag{6}$$

The largest rank k satisfying $p_{(k)} \le \frac{k}{m}\alpha$.

Was identified, and the corresponding tests were considered significant after FDR correction.

The Benjamini-Hochberg correction was applied separately for each parameter and each population comparison across the 1441 time instants. This procedure yielded a temporal significance mask indicating the time instants at which the differences between the compared populations remained statistically significant after multiple-comparison correction.

3. Results

3.1. Data Availability

In this study, we had access to GNSS observation data initially covering the 2010-2017 period, corresponding to eight years (2922 theoretical days). Of the 2922 theoretically available days, observations were recorded for 1886 days, corresponding to an overall data availability of 64.54%. The remaining 1036 days, representing 35.46% of the period, correspond to data-gap days, characterized by the complete absence of ROTI data.

Data availability nevertheless exhibits substantial year-to-year variability. The year 2017 is particularly characterized by a high proportion of data-gap days. Dif-

ferences in data availability are also observed across seasons. Over the entire 2010-2017 period, data availability is highest in winter and spring, with 79.50% and 78.72%, respectively, of the theoretically expected days having observations. ROTI data availability was relatively lower in autumn (64.91%) and particularly in summer (59.16%). All four seasons are nevertheless represented throughout the period considered, with data coverage exceeding 50%.

Given the low data availability in 2017, the climatological analysis of ionospheric irregularities is restricted to the 2010-2016 period. This period comprises 2557 theoretically available days, of which 1757 days have observations, corresponding to a data availability of 68.71%. The remaining 800 days correspond to data gaps, representing 31.29% of the period. The 2010-2016 period therefore constitutes the temporal basis retained for the remainder of this study.

3.2. Climatological Study of Ionospheric Irregularities at the Koudougou GNSS Station

3.2.1. Overall Occurrence of Ionospheric Irregularities

The occurrence frequency of ionospheric irregularities was assessed using the available GNSS observations over the 2010-2016 period. A total of 1757 days with valid observations were retained for the analysis. Among these days, 1107 exhibited ROTI values equal to or greater than 0.5 TECU/min, corresponding to an occurrence rate of 63.00% of the days with available data.

The days with ionospheric irregularities were then classified according to their intensity (**Figure 2(a)**). Moderate episodes ($0.5 \le \mathrm{ROTI}_{max} \le 1\,\mathrm{TECU/min}$) were observed on 484 days, corresponding to 43.72% of the days with irregularities, whereas strong episodes ($\mathrm{ROTI}_{max} > 1\,\mathrm{TECU/min}$)were observed on 623 days, corresponding to 56.28%. Strong episodes therefore accounted for the highest proportion of days with ionospheric irregularities.

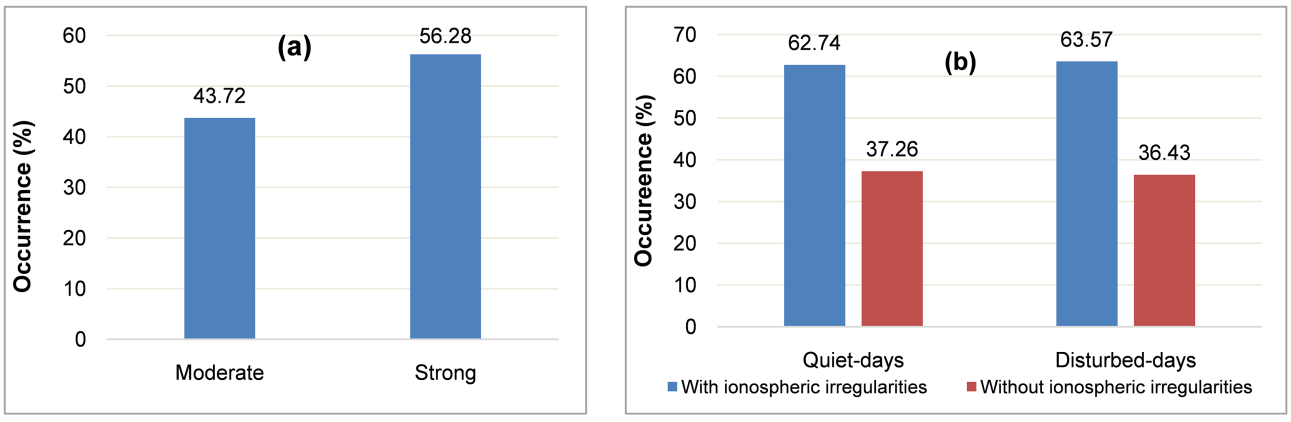


Figure 2. Occurrence of days with ionospheric irregularities at the Koudougou GNSS station during the 2010-2016 period. (a) According to episode intensity; (b) According to geomagnetic conditions.

The geomagnetic context associated with days exhibiting ionospheric irregularities was also examined (**Figure 2(b)**). For each category, the occurrence fre-

quency was calculated as the ratio of the number of days with irregularities to the total number of days with available observations. Under geomagnetically quiet conditions ($Aa < 20$ nT), irregularities were observed on 751 of the 1197 available days, corresponding to an occurrence frequency of 62.74%. Under disturbed conditions ($Aa \geq 20$ nT), they occurred on 356 of 560 available days, yielding a frequency of 63.57%. Furthermore, among the 1107 days with irregularities during the 2010-2016 period, 67.84% occurred under quiet conditions, and 32.16% under disturbed conditions.

3.2.2. Diurnal Occurrence of Ionospheric Irregularities

The diurnal distribution of ionospheric irregularities was examined using the 1107 days with ionospheric irregularities identified during the 2010-2016 period. Among these days, 193 days (17.43%) corresponded to daytime occurrences, whereas 914 days (82.57%) corresponded to nighttime occurrences.

The diurnal distribution was then examined according to episode intensity (Figure 3). Of the 484 days with moderate episodes, 174 daytime days (35.95%) and 310 nighttime days (64.05%) were observed. For 623 days with strong episodes, 19 days (3.05%) corresponded to daytime occurrences, compared with 604 days (96.95%) corresponding to nighttime occurrences.

Nighttime was defined as the interval between 18:00 and 06:00 LT. The observations show that nighttime ionospheric irregularities were mainly concentrated between 18:00 and 02:00 LT.

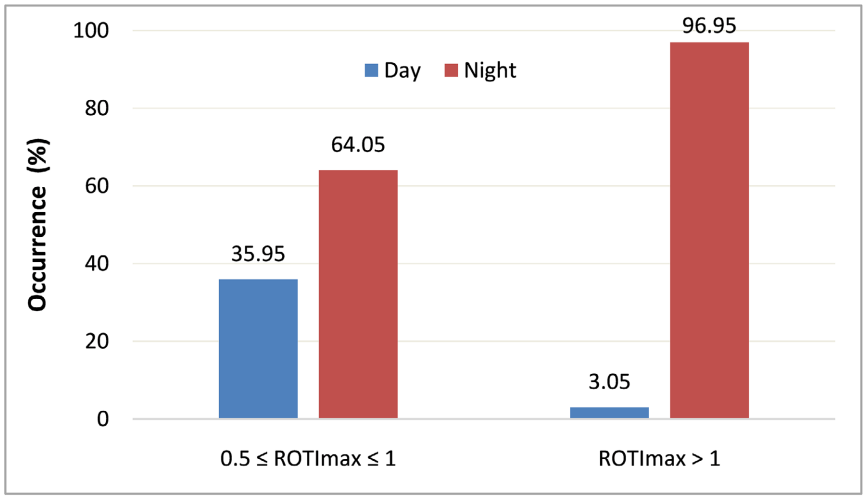


Figure 3. Diurnal distribution of ionospheric irregularities at the Koudougou GNSS station during the 2010-2016 period, according to episode intensity.

3.2.3. Seasonal Occurrence of Ionospheric Irregularities

Figure 4 shows the seasonal occurrence rates of ionospheric irregularities at the Koudougou GNSS station during the 2010-2016 period. These rates were calculated by relating the number of irregularity days to the total number of observation days available for each season. The highest occurrences were observed in spring (335 irregularity days out of 414 observation days, corresponding to

80.92%), followed by autumn (305/418 days, corresponding to 72.97%). In winter, 272 irregularity days were recorded out of 481 observation days (56.55%), whereas summer exhibited the lowest occurrence, with 195 irregularity days out of 444 observation days (43.92%).

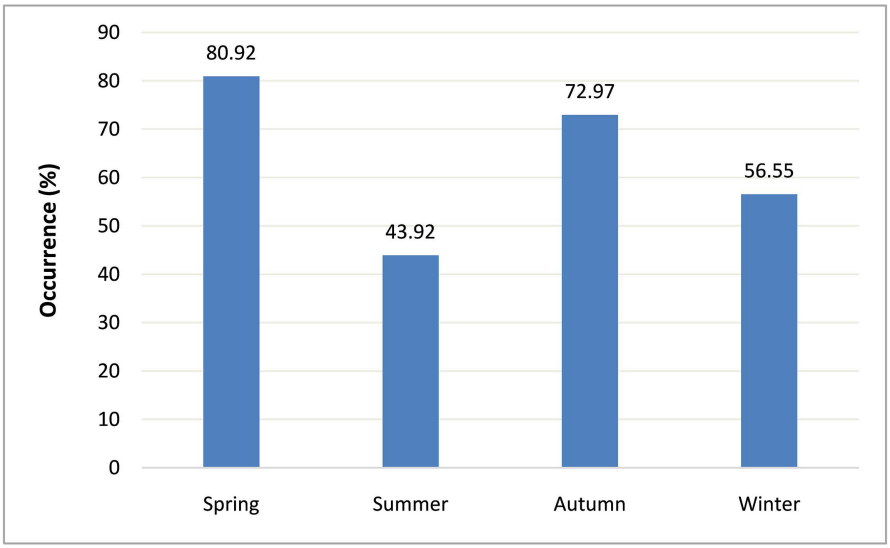


Figure 4. Seasonal occurrence of ionospheric irregularities at the Koudougou GNSS station during the 2010-2016 period.

3.3. Interplanetary Conditions Associated with Ionospheric Irregularity Episodes

Interplanetary conditions associated with episodes of ionospheric irregularities were examined using Superposed Epoch Analysis (SEA), applied to moderate and strong episodes. For each intensity level, the temporal profiles of B_{mag}, B_z, V, and P_{dyn} were compared across quiet, transition, and disturbed geomagnetic context categories. The time series were aligned to the onset of each episode as $t_0 = 0$ and analyzed within a time window spanning −12 h to +12 h around $t_0 = 0$, at one-minute resolution, yielding 1441 data points per episode. At each time step, differences between the transition category and the quiet and disturbed categories were assessed using Welch's test. A multiple-comparison correction based on the Benjamini-Hochberg (FDR) procedure, with $\alpha = 0.05$, was then applied for each parameter and comparison across the entire set of 1441 time steps.

3.3.1. Strong Episodes

The profiles of B_{mag}, V, and P_{dyn} show a similar organization among the three categories (**Figure 5(a)**, **Figure 5(c)**, and **Figure 5(d)**). For these parameters, the values observed during strong-disturbed (SD) are higher than those observed during strong-transition (ST) episodes, which in turn are higher than those observed during strong-quiet (SQ) episodes. This general order, SD > ST > SQ, is observed throughout the time window considered. The B_z profile exhibits a different configuration (**Figure 5(b)**). The values associated with SQ remain slightly positive,

those for ST are close to zero, whereas those for SD are negative.

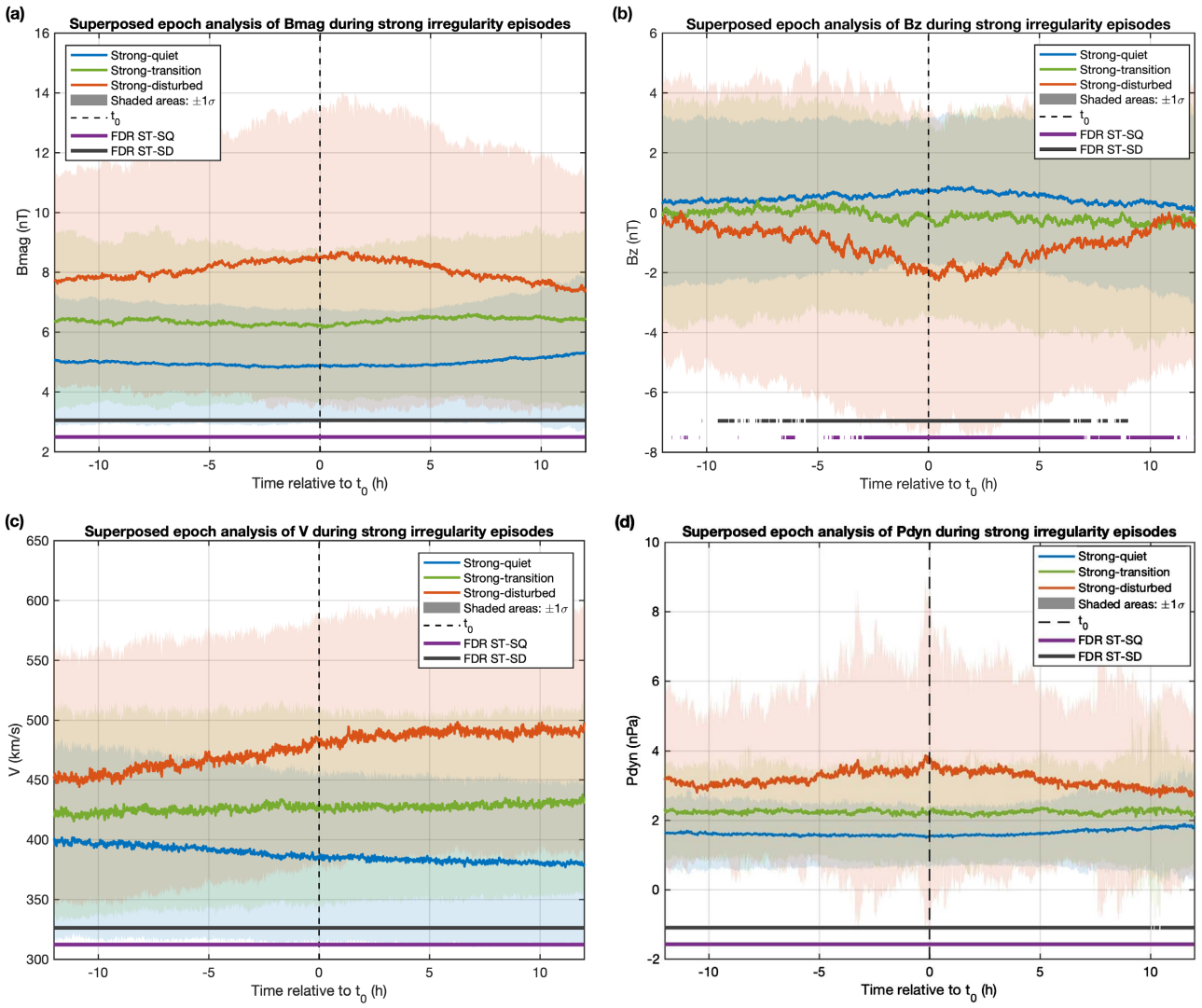


Figure 5. Superposed epoch analysis of interplanetary parameters during strong ionospheric irregularity episodes at the Koudougou GNSS station during the 2010-2016 period: (a) B_{mag}, (b) B_z, (c) solar-wind speed V; and (d) dynamic pressure P_{dyn}. Blue, green, and orange curves represent strong-quiet, strong-transition, and strong-disturbed episodes, respectively; shaded areas indicate $\pm 1\sigma$. The vertical dashed line marks t_0, the episode onset. Horizontal bars indicate significant differences between ST and SQ and ST and SD after Benjamini-Hochberg FDR correction ($\alpha = 0.05$).

Table 2 summarizes the observations at t_0. B_{mag}, B_z, and P_{dyn} show particularly pronounced separation among the three populations. For B_{mag} and P_{dyn}, the values generally follow the ordering SQ < ST < SD over the entire time window. The B_z profile shows a distinct organization, with SQ values remaining slightly positive, ST values close to zero, and SD values negative. The V profile shows a progressive decrease for SQ, whereas the ST and, particularly, SD values increase over the time window.

Over the entire time window, the differences between ST and SQ are significant after FDR correction at 1441/1441 time points for B_{mag}, V, and P_{dyn}, and

952/1441 time points for B_z. For the ST-SD comparison, FDR significance is observed at 1441/1441 time points for B_{mag}, and V, at 1006/1441 time points for B_z, and at 1437/1441 time points for P_{dyn}.

Table 2. Solar-wind parameter values at $t = 0$ h for strong episodes.

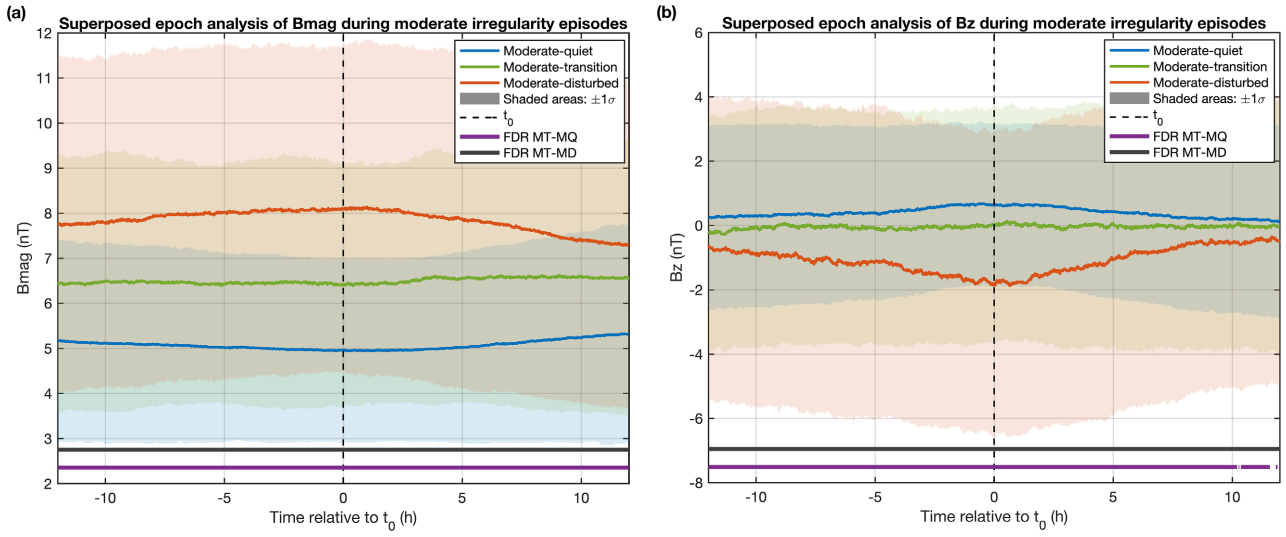
Parameter	Strong-quiet	Strong-transition	Strong-disturbed	ST-SQ	ST-SD	FDR ST-SQ	FDR ST-SD
B_{mag} (nT)	4.87 ± 1.94	6.22 ± 2.54	8.51 ± 4.95	+1.35	−2.30	1441/1441	1441/1441
B_z (nT)	0.80 ± 2.39	−0.21 ± 3.22	−1.98 ± 5.50	−1.01	+1.78	952/1441	1006/1441
V (km/s)	384.48 ± 71.56	426.81 ± 81.16	480.17 ± 103.64	+42.33	−53.36	1441/1441	1441/1441
P_{dyn} (nPa)	1.52 ± 0.88	2.16 ± 1.26	3.65 ± 4.69	+0.64	−1.48	1441/1441	1437/1441

3.3.2. Moderate Episodes

Moderate episodes (Figure 6) exhibit the same organizational patterns observed in strong episodes. Throughout the time window, the profiles of B_{mag}, V, and P_{dyn} follow the general hierarchy moderate-disturbed (MD) > moderate-transition (MT) > (MQ) moderate-quiet (Figure 6(a), Figure 6(c), and Figure 6(d)). The B_z profile exhibits a different configuration (Figure 6(b)): the values associated with MQ are positive, those for MT are close to zero, whereas those for MD are negative.

Table 3 summarizes the observations at t_0. As with strong episodes, the B_{mag}, B_z, and P_{dyn} parameters show particularly pronounced separation among the three populations at t_0. The V profile shows a slight decrease for MQ, whereas the MT and, particularly, MD values increase over the time window.

Over the entire time window, the differences between MT and MQ are significant after FDR correction at 1441/1441 time points for B_{mag}, V, and P_{dyn}, and at 1420/1441 time points for B_z. For the MT-MD comparison, FDR significance is observed at 1441/1441 time points for all four parameters.



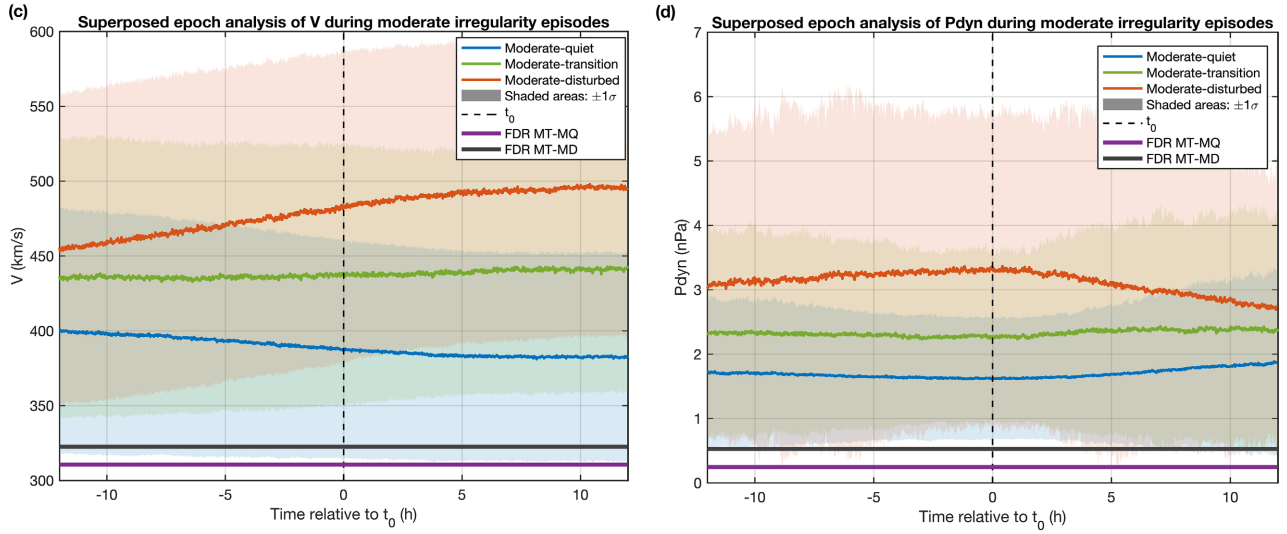


Figure 6. Superposed epoch analysis of interplanetary parameters during moderate ionospheric irregularity episodes at the Koudougou GNSS station during the 2010-2016 period: (a) B_{mag}, (b) B_z, (c) solar-wind speed V; and (d) dynamic pressure P_{dyn}. Blue, green, and orange curves represent moderate-quiet, moderate-transition, and moderate-disturbed episodes, respectively; shaded areas indicate $\pm 1\sigma$. The vertical dashed line marks t_0, the episode onset. Horizontal bars indicate significant differences between MT and MQ and MT and MD after Benjamini-Hochberg FDR correction ($\alpha = 0.05$).

Table 3. Solar-wind parameter values at $t = 0$ h for moderate episodes.

Parameter	Moderate-quiet	Moderate-transition	Moderate-disturbed	MT-MQ	MT-MD	FDR MT-MQ	FDR MT-MD
B_{mag} (nT)	4.96 ± 2.04	6.42 ± 2.67	8.09 ± 3.58	+1.4626	−1.67	1441/1441	1441/1441
B_z (nT)	0.65 ± 2.52	−0.03 ± 3.65	−1.82 ± 5.50	−0.6214	+1.84	1420/1441	1441/1441
V (km/s)	387.84 ± 72.66	438.22 ± 87.04	483.46 ± 103.80	+50.376	−45.24	1441/1441	1441/1441
P_{dyn} (nPa)	1.62 ± 0.94	2.26 ± 1.28	3.31 ± 2.44	+0.6383	−1.05	1441/1441	1441/1441

4. Discussion

4.1. Occurrence and Variability of Ionospheric Irregularities

The climatological analysis at Koudougou, during 2010-2016 period, shows that ionospheric irregularities were observed on 1107 of the 1757 days with available observations, corresponding to an occurrence frequency of 63.00%. Among these days, 43.72% corresponded to moderate irregularities and 56.28% to strong irregularities. This frequency indicates that irregularities are a recurrent phenomenon at the Koudougou GNSS station during the 2010-2016 period. It is consistent with the strong longitudinal and temporal variability of equatorial ionospheric irregularities reported by [8], as well as with the variations among stations and periods documented over East Africa using GNSS/ROTI observations [25].

The diurnal distribution reveals a clear nighttime predominance of ionospheric

irregularities at Koudougou. Among the 1107 days with irregularities, 914 days (82.57%) corresponded to nighttime occurrences, compared with 193 days (17.43%) for daytime occurrences. Irregularities were mainly concentrated between 18:00 and 02:00 LT, consistent with observations reported in other equatorial African regions based on ROTI, which generally show a dominant occurrence during post-sunset and pre-midnight sectors [13]-[15]. This temporal pattern is consistent with the particular post-sunset electrodynamic conditions, including the prereversal enhancement of the zonal electric field and the uplift of the F region, which provide favorable conditions for the development of the Rayleigh-Taylor instability. However, the ROTI data used here do not allow the electric field or the $E \times B$ drift to be measured directly.

The analysis of seasonal variability shows that ionospheric irregularities occur preferentially during the equinoctial seasons. The occurrence rates obtained in spring (80.92%) and autumn (72.97%) are significantly higher than those observed in winter (56.55%) and summer (43.92%). This pattern is broadly consistent with observations reported in other African regions based on ROTI, which generally show higher irregularity occurrence during the equinoxes than during the solstices [10] [13]. Recent observations over East Africa likewise show higher occurrence during the equinoctial months [25]. This pattern is also consistent with observations from Koudougou and Ouagadougou, which show enhanced ROTI activity around the equinoctial months [18].

The occurrence rates of ionospheric irregularities observed under geomagnetically quiet (62.74%) and disturbed (63.57%) conditions are very similar, with a difference of only 0.83 percentage points, suggesting a limited dependence of their occurrence on the overall level of geomagnetic activity. This result differs from that reported by [25], who found higher occurrence rates of equatorial plasma bubbles under quiet than under disturbed conditions at four stations in East Africa. This discrepancy may be related to differences in the phenomena investigated, the criteria used to identify irregularities, and the observation regions. Finally, 67.84% of the days with irregularities occurred under quiet conditions; this proportion should be interpreted in light of the number of observation days available in each geomagnetic category.

4.2. Interplanetary Conditions Associated with Ionospheric Irregularity Episodes

The analysis of interplanetary conditions reveals a consistent organization of solar wind parameters according to the geomagnetic context associated with ionospheric irregularity episodes. For both strong and moderate episodes, B_{mag}, V, and P_{dyn}, progressively increase from quiet to transition and then disturbed conditions, whereas B_z evolves from slightly positive values (quiet episodes) toward values close to zero (transition episodes) and then negative values (disturbed episodes). This organization, observed throughout the entire time window, is supported by the statistically significant differences obtained after FDR correction. It indicates that the ionospheric irregularity episodes observed at Koudougou are

associated with interplanetary conditions that vary systematically with the level of geomagnetic disturbance.

The behavior of B_z is particularly relevant to the interpretation of solar wind-magnetosphere coupling. The transition from slightly positive values under quiet conditions to negative values under disturbed conditions indicates a progressively more southward orientation of the interplanetary magnetic field. Southward B_z can favor magnetic reconnection on the dayside and thereby enhance the transfer of energy from the solar wind to the magnetosphere. This interaction can modify electric fields and magnetospheric convection, with subsequent effects on ionospheric electrodynamics. In equatorial regions, prompt penetration electric fields (PPEFs) and, on longer timescales, disturbance dynamo electric fields (DDEFs) can modify the vertical $E \times B$ drift and the conditions favorable for the development of F-region irregularities [6] [26]-[28]. Although the ROTI data used here do not directly measure either electric fields or the $E \times B$ drift, this interpretation therefore provides a physical framework for understanding the observed association, rather than direct evidence of a causal mechanism at Koudougou.

The solar wind speed and dynamic pressure also show a progressive increase from quiet to disturbed conditions. This evolution indicates that episodes associated with disturbed geomagnetic conditions occur within a more dynamic solar wind environment. Dynamic pressure is particularly relevant because it reflects the intensity of the forcing exerted by the solar wind on the magnetosphere. Superposed epoch analyses based on GNSS observations have shown that variations in P_{dyn} can be associated with changes in the ionospheric response during geomagnetic storms [29]. In our case, however, the increase in P_{dyn} is accompanied by variations in B_{mag}, V, B_z, preventing the observed differences from being attributed to a single interplanetary parameter.

Finally, the presence of a transition population between quiet and disturbed conditions, for both intensity levels, is associated with intermediate composite values of the solar wind and IMF parameters. In particular, B_{mag}, solar wind speed, and dynamic pressure progressively increase from the quiet to the disturbed category, while B_z evolves from predominantly positive values to near-zero and then negative values. This organization suggests a continuum of interplanetary driving conditions across the three categories. However, because the transition category is defined by mixed geomagnetic activity within the classification window, it should not be interpreted as direct evidence of a gradual temporal evolution of individual events.

It should nevertheless be emphasized that the differences observed between the groups defined by geomagnetic activity are, at least partly, consistent with the well-established coupling between the solar wind and geomagnetic activity. Therefore, the associations identified between solar wind parameters and ionospheric irregularity episodes should be interpreted within the broader context of solar the wind-magnetosphere-ionosphere coupling system. Finally, a potential

limitation of this study is that closely spaced episodes may not be fully independent in the SEA framework because of overlapping solar wind intervals. While a minimum separation of 15 minutes was imposed between successive events, the effect of this residual dependence remains to be assessed.

5. Conclusions and Perspectives

This study characterized ionospheric irregularities observed at the Koudougou GNSS station during the 2010-2016 period. The results show a predominantly nighttime occurrence and seasonal variability, with the largest occurrences of irregularity days occurring in spring and autumn. Ionospheric irregularity episodes were observed under both quiet and disturbed geomagnetic conditions. The analysis of interplanetary conditions revealed a consistent organization of the solar-wind parameters among the quiet, transition, and disturbed populations, for both moderate and strong episodes.

These results demonstrate the value of combining GNSS/ROTI observations with geomagnetic context and interplanetary conditions to characterize the variability of ionospheric irregularities at Koudougou. However, ROTI does not directly measure the electrodynamic processes involved in their development. Complementary observations of ionospheric and electrodynamic parameters, together with improved temporal data coverage, will help further investigate the mechanisms underlying these irregularities and their dependence on geophysical conditions.

Acknowledgements

The authors are grateful to the Mines-Télécom Institute for setting up the Koudougou GPS station. They also thank the use of NASA/GSFC's Space Physics Data Facility OMNIWeb service and OMNI data and the International Service of Geomagnetic Indices (ISGI) and collaborating institutes for providing geomagnetic indices. Furthermore, the authors acknowledge the GIRGEA (Groupement de Recherche International en Géophysique Europe-Afrique) for providing open access to the software package used in this study for ROTI data processing and analysis.

Author Contributions

All authors contributed substantially to the conception of the study, the analysis and interpretation of results, and the preparation of the manuscript. All authors reviewed and approved the final version of the manuscript.

Conflicts of Interest

The authors declare no conflicts of interest.

References

[1] Coster, A.J. and Yizengaw, E. (2021) GNSS/GPS Degradation from Space Weather. In: Coster, A.J., Erickson, P.J., Lanzerotti, L.J., Zhang, Y. and Paxton, L.J., Eds., *Space*

Weather Effects and Applications, Wiley, 165-181. https://doi.org/10.1002/9781119815570.ch8

[2] Abdu, M.A. (2001) Outstanding Problems in the Equatorial Ionosphere-Thermosphere Electrodynamics Relevant to Spread F. *Journal of Atmospheric and Solar-Terrestrial Physics*, **63**, 869-884. https://doi.org/10.1016/s1364-6826(00)00201-7

[3] Abdu, M.A. (2016) Electrodynamics of Ionospheric Weather over Low Latitudes. *Geoscience Letters*, **3**, Article No. 11. https://doi.org/10.1186/s40562-016-0043-6

[4] Fejer, B.G. and Kelley, M.C. (1980) Ionospheric Irregularities. *Reviews of Geophysics*, **18**, 401-454. https://doi.org/10.1029/rg018i002p00401

[5] Fejer, B.G., Scherliess, L. and de Paula, E.R. (1999) Effects of the Vertical Plasma Drift Velocity on the Generation and Evolution of Equatorial Spread *f*. *Journal of Geophysical Research*: *Space Physics*, **104**, 19859-19869. https://doi.org/10.1029/1999ja900271

[6] Abdu, M.A. (2012) Equatorial Spread F/Plasma Bubble Irregularities under Storm Time Disturbance Electric Fields. *Journal of Atmospheric and Solar-Terrestrial Physics*, **75**, 44-56. https://doi.org/10.1016/j.jastp.2011.04.024

[7] Kintner, P.M., Ledvina, B.M. and de Paula, E.R. (2007) GPS and Ionospheric Scintillations. *Space Weather*, **5**, S09003. https://doi.org/10.1029/2006sw000260

[8] Yizengaw, E. and Groves, K.M. (2018) Longitudinal and Seasonal Variability of Equatorial Ionospheric Irregularities and Electrodynamics. *Space Weather*, **16**, 946-968. https://doi.org/10.1029/2018sw001980

[9] Pi, X., Mannucci, A.J., Lindqwister, U.J. and Ho, C.M. (1997) Monitoring of Global Ionospheric Irregularities Using the Worldwide GPS Network. *Geophysical Research Letters*, **24**, 2283-2286. https://doi.org/10.1029/97gl02273

[10] Mungufeni, P., Habarulema, J.B. and Jurua, E. (2016) Trends of Ionospheric Irregularities over African Low Latitude Region during Quiet Geomagnetic Conditions. *Journal of Atmospheric and Solar-Terrestrial Physics*, **138**, 261-267. https://doi.org/10.1016/j.jastp.2016.01.015

[11] Olwendo, J.O., Cilliers, P., Weimin, Z., Ming, O. and Yu, X. (2018) Validation of ROTI for Ionospheric Amplitude Scintillation Measurements in a Low-Latitude Region over Africa. *Radio Science*, **53**, 876-887. https://doi.org/10.1029/2017rs006391

[12] Olwendo, J., Cilliers, P.J. and Ming, O. (2021) Monthly Trends in Temporal and Spatial Distribution of Ionospheric Irregularities across the African Region during the Descending Phase of Solar Cycle 24. *Advances in Space Research*, **67**, 3187-3201. https://doi.org/10.1016/j.asr.2021.01.052

[13] Adebiyi, S.J., Ikubanni, S.O., Bolaji, O.S., Fashae, J.B., Adebesin, B.O., Joshua, B.W., *et al*. (2021) Equatorial F-Region Irregularities at Different Seasons in Africa. *Advances in Space Research*, **68**, 1850-1863. https://doi.org/10.1016/j.asr.2021.04.025

[14] Amaechi, P.O., Oyeyemi, E.O., Akala, A.O. and Amory-Mazaudier, C. (2020) Geomagnetic Activity Control of Irregularities Occurrences over the Crests of the African Eia. *Earth and Space Science*, **7**, e2020EA001183. https://doi.org/10.1029/2020ea001183

[15] Bolaji, O.S., Adebiyi, S.J., Fashae, J.B., Ikubanni, S.O., Adenle, H.A. and Owolabi, C. (2020) Pattern of Latitudinal Distribution of Ionospheric Irregularities in the African Region and the Effect of March 2015 St. Patrick's Day Storm. *Journal of Geophysical Research*: *Space Physics*, **125**, e2019JA027641. https://doi.org/10.1029/2019ja027641

[16] Sawadogo, S., Gnabahou, D.A., Pahima, T. and Ouattara, F. (2023) Total Electron Content during Recurrent and Quiet Geomagnetic Periods at the Koudougou Station

in Burkina Faso. *International Journal of Astronomy and Astrophysics*, **13**, 259-280. https://doi.org/10.4236/ijaa.2023.133015

[17] Tapsoba, E.V., Fleury, R., Sawadogo, E.W., Gnabahou, A.D. and Ouattara, F. (2026) Temporal Distribution of EPBs Occurrence Using Seven West African GPS Stations. *Applied Physics Research*, **18**, 216-230. https://doi.org/10.5539/apr.v18n1p216

[18] Emmanuel, S.W., Salfo, K., Mathieu, B., Pouraogo, O., Christian, Z., Jean-Louis, Z., *et al*. (2026) Ionospheric Phase Scintillation during Solar Cycle 24 over West Africa: Analysis from GPS Stations at Koudougou and Ouagadougou (BF01). *Current Journal of Applied Science and Technology*, **45**, 28-40. https://doi.org/10.9734/cjast/2026/v45i14650

[19] Jacobsen, K.S. and Dähnn, M. (2014) Statistics of Ionospheric Disturbances and Their Correlation with GNSS Positioning Errors at High Latitudes. *Journal of Space Weather and Space Climate*, **4**, A27. https://doi.org/10.1051/swsc/2014024

[20] Wang, C., Min, X. and Hu, H. (2025) An Ionospheric Disturbed Index Based on Roti. *Space Weather*, **23**, e2025SW004445. https://doi.org/10.1029/2025sw004445

[21] Liu, X., Yuan, Y., Tan, B. and Li, M. (2016) Observational Analysis of Variation Characteristics of GPS-Based TEC Fluctuation over China. *ISPRS International Journal of Geo-Information*, **5**, Article 237. https://doi.org/10.3390/ijgi5120237

[22] Legrand, J.P. and Simon, P.A. (1989) Solar Cycle and Geomagnetic Activity: A Review for Geophysicists. Part I. The Contributions to Geomagnetic Activity of Shock Waves and of the Solar Wind. *Annales Geophysicae*, **7**, 565-578.

[23] Ouattara, F. and Amory-Mazaudier, C. (2009) Solar-Geomagnetic Activity and Aa Indices toward a Standard Classification. *Journal of Atmospheric and Solar-Terrestrial Physics*, **71**, 1736-1748. https://doi.org/10.1016/j.jastp.2008.05.001

[24] Zerbo, J.L., Amory Mazaudier, C., Ouattara, F. and Richardson, J.D. (2012) Solar Wind and Geomagnetism: Toward a Standard Classification of Geomagnetic Activity from 1868 to 2009. *Annales Geophysicae*, **30**, 421-426. https://doi.org/10.5194/angeo-30-421-2012

[25] Alemu, Z. and Kassa, T. (2025) Investigation of Equatorial Plasma Bubble Irregularities under Quiet and Disturbed Geomagnetic Conditions over the East African Longitudinal Sector in 2015. *Advances in Space Research*, **75**, 3671-3691. https://doi.org/10.1016/j.asr.2024.12.012

[26] Fejer, B.G., Jensen, J.W., Kikuchi, T., Abdu, M.A. and Chau, J.L. (2007) Equatorial Ionospheric Electric Fields during the November 2004 Magnetic Storm. *Journal of Geophysical Research*: *Space Physics*, **112**, A10304. https://doi.org/10.1029/2007ja012376

[27] Kelley, M.C. (2009) The Earth's Ionosphere: Plasma Physique and Electrodynamics. 2nd Edition, Academic Press.

[28] Amaechi, P.O., Oyeyemi, E.O., Akala, A.O., Messanga, H.E., Panda, S.K., Seemala, G.K., *et al*. (2021) Ground-Based GNSS and C/NOFS Observations of Ionospheric Irregularities over Africa: A Case Study of the 2013St. Patrick's Day Geomagnetic Storm. *Space Weather*, **19**, e2020SW002631. https://doi.org/10.1029/2020sw002631

[29] Sori, T., Shinbori, A., Otsuka, Y., Nishioka, M. and Perwitasari, S. (2023) Dependence of Ionospheric Responses on Solar Wind Dynamic Pressure during Geomagnetic Storms Using Global Long-Term GNSS-TEC Data. *Journal of Geophysical Research*: *Space Physics*, **128**, e2022JA030913. https://doi.org/10.1029/2022ja030913